




# Self-Sensing Cellulose Structures With Design-Controlled Stiffness

Fabian Wiesemüller , Crystal Winston , Alexandre Poulin, Xavier Aeby, Aslan Miriyev, Thomas Geiger, Gustav Nyström, and Mirko Kovač , *Member, IEEE*

**Abstract**—Robots are often used for sensing and sampling in natural environments. Within this area, soft robots have become increasingly popular for these tasks because their mechanical compliance makes them safer to interact with. Unfortunately, if these robots break while working in vulnerable environments, they create potentially hazardous waste. Consequently, the development of compliant, biodegradable structures for soft, eco-robots is a relevant research area that we explore here. Cellulose is one of the most abundant biodegradable materials on earth, but it is naturally very stiff, which makes it difficult to use in soft robots. Here, we look at both biologically and kirigami inspired structures that can be used to reduce the stiffness of cellulose based parts for soft robots up to a factor of 19 000. To demonstrate this, we build a compliant force and displacement sensing structure from microfibrillated cellulose. We also describe a novel manufacturing technique for these structures, provide mechanical models that allow designers to specify their stiffness, and conclude with a description of our structure’s performance.

**Index Terms**—Compliant joint/mechanism, soft robot materials and design, soft sensors and actuators.

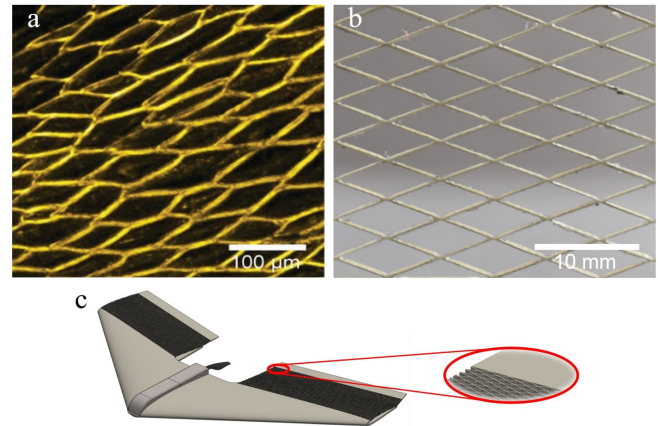


Fig. 1. Microscope images of an ice plant *Delosperma nakurense* seed showing a similar geometry as our proposed compliant structure. The same geometry integrated into a camber-morphing wing. a) Confocal image of a hydro-actuated seed capsule of an ice seed plant taken from [1] with permission of Springer Nature. b) Macro-image of the manufactured compliant cellulose honeycomb structure ( $\theta = 22.5^\circ$ ). c) Example of how these structures would be integrated in a bio-hybrid degradable morphing flying wing with a detailed view of the honeycomb elements ( $\theta = 22.5^\circ$ ).

Manuscript received October 23, 2020; accepted February 16, 2021. Date of publication March 18, 2021; date of current version April 6, 2021. This letter was recommended for publication by Associate Editor G.Gu and Kyu-Jin Cho upon evaluation of the reviewers’ comments. This work was supported in part by EPSRC Awards EP/R009953/1, EP/L016230/1, and EP/R026173/1, in part by NERC Award NE/R012229/1, in part by the EU H2020 AeroTwin project under Grant ID 810321, and in part by the Empa-Imperial research partnership. (*Corresponding authors: Fabian Wiesemuller; Mirko Kovac.*)

Fabian Wiesemüller, Aslan Miriyev, and Mirko Kovač are with the Materials and Technology Center of Robotics, Empa - Swiss Federal Laboratories for Materials Science and Technology, 8600 Dübendorf, Switzerland and also with the Aerial Robotics Laboratory, Imperial College London, South Kensington Campus, London, SW7 2AZ, U.K. (e-mail: fabian.wiesemuller@empa.ch; aslan.miriyev@empa.ch; mirko.kovac@empa.ch).

Crystal Winston is with the Aerial Robotics Laboratory, Imperial College London, South Kensington Campus, London SW7 2AZ, U.K. (e-mail: c.winston19@imperial.ac.uk).

Alexandre Poulin, Xavier Aeby, and Thomas Geiger are with the Laboratory for Cellulose & Wood Materials, Empa - Swiss Federal Laboratories for Materials Science and Technology, 8600 Dübendorf, Switzerland (e-mail: alexandre.poulin@empa.ch; xavier.aeby@empa.ch; thomas.geiger@empa.ch).

Gustav Nyström is with the Laboratory for Cellulose & Wood Materials, Empa - Swiss Federal Laboratories for Materials Science and Technology, 8600 Dübendorf, Switzerland and also with the Department of Health Sciences and Technology, ETH Zürich, 8092 Zürich, Switzerland (e-mail: gustav.nystroem@empa.ch).

This letter has supplementary downloadable material available at <https://doi.org/10.1109/LRA.2021.3067243>, provided by the authors.

Digital Object Identifier 10.1109/LRA.2021.3067243

## I. INTRODUCTION

CELLULOSE is one of the most abundant materials on Earth. Its biodegradability and capability for functionalization also make it an ideal material for biodegradable eco-robots. These are robots that can operate in natural environments, and, if they break, degrade without producing waste. This paper studies approaches to designing self sensing structures with design-controlled stiffness made from microfibrillated cellulose (MFC) which can be soft robotic building blocks for eco-robots. Here, we focus on the structural design of compliance into biodegradable materials and the integration of self-sensing capabilities with the use of a conductive ink.

In nature, ice plants (*Delosperma nakurense* (Engl.) Herre) use a flexible honeycomb micro-structure to unfold and release its seeds [1]. An image of the ice plant capsule’s honeycomb structure is given in Fig. 1a. In this paper we apply a similar method to change the compliance of MFC structures. Fig. 1(b) shows an image of the proposed honeycomb structure. The system described is an investigation into an internal structure for a self-sensing, biodegradable, camber-morphing wing, like the one shown in Fig. 1(c). Typically, fixed wing vehicles use control surfaces, moved by hinges, in order to control the vehicle. However, the gap in the wing caused by the deflection of these

surfaces increases drag and decreases energetic efficiency. Using a flexible internal structure, like the one investigated here, may allow for more efficient roll control of the vehicle, while avoiding the use of traditional hinges, bolts or rivets. Functionalizing it with self-sensing capabilities can provide feedback for controlling the wing's camber. This said, the functionalization and stiffness design of these structures can be used for a wide variety of other soft biodegradable robots.

The MFC plates used here have an elongation at break  $\epsilon_b$  of 1.05% and a Young's modulus ranging from 2 GPa–4 GPa, which is far too stiff for a soft and stretchable robot without some form of structural modification. This is a problem that researchers have encountered with several other materials when trying to make soft robots, and two popular solutions are to use either honeycomb or kirigami structures to reduce and design the stiffness of the geometry for a particular application.

Kirigami is a variation of origami that involves cutting slits into sheets of material to change their shape and/or mechanical properties, while honeycombs are lattices of geometric cells that can reduce the stiffness of a structure through bending within their cell walls. Both of these structures have been used for flexible strain sensing [2]–[7], energy harvesting [8] or actuation [9]–[15] applications because they allow engineers to design the stiffness based on how cuts are made in the material. Numerical and analytical models describing the mechanical properties of certain kirigami and honeycomb structures have also been developed [15]–[17]. The presented references have mostly focused on the design and manufacturing of kirigami and origami structures made from 2-dimensional sheets of material. With this research, we aim to work towards the manufacturing of compliant structures made from ice-templated MFC with a design controlled thickness to enable integration as a structural element with embedded sensing for flying robot wings. MFC features a unique combination of light weight, mechanical strength and compatibility for 3D manufacturing and is seen as the ideal material for aerial soft robotics.

The primary differences between honeycomb and kirigami structures are the trade-off between stiffness and weight. The kirigami structure is less stiff than the honeycomb structure, as shown in Fig. 2. Furthermore, as the angle of the honeycomb structure increases, so does its stiffness. However, the kirigami structure yields virtually no reduction in weight, while the diamond-celled honeycomb does. This behavior is characterized by the formula  $\bar{\rho} = \frac{2t}{l \sin(2\theta)}$  given by [18], where  $\bar{\rho}$  is the relative density between the honeycomb and the material it is made from.  $2\theta$  describes the angle between the cell walls.

Given that this is a preliminary investigation into a biodegradable structure for a morphing wing, the trade-offs between both stiffness and weight were considered before the final geometry for integrating self-sensing capabilities was selected.

Various plants are capable of sensing and responding to environmental stimuli like moisture, light, temperature, and mechanical perturbations [19], [20]. This intelligent capability of changing the morphology in response to a given trigger is known as plant perception [21], [22] and can be used as a template for designing a cellulose structure with self-sensing capabilities. In general, diverse options for integrating sensing (resistive [23], piezoresistive [24], capacitive [25], optical [26]) into a material

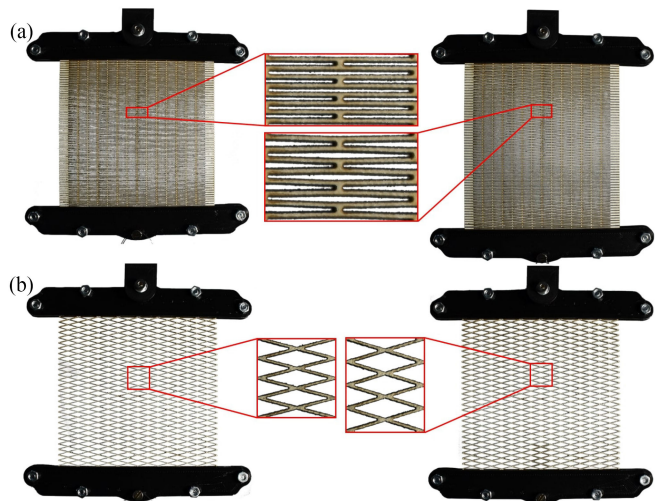


Fig. 2. Comparison of stiffness between kirigami and a diamond-celled honeycomb structure at 200 grams loading. Left column showing the structure unloaded, right column showing the structure loaded with a total displacement of 11 mm. a) Kirigami structure with a total displacement of 11 mm. b) Honeycomb structure ( $\theta = 15.0^\circ$ ) with a total displacement of 2 mm.

are available, nevertheless not all of them are appropriate for designing a biodegradable, flexible and lightweight structure. In this work we have focused on resistive measurements of strain, since this type of sensing could be used to provide feedback for camber morphing control and is fairly simple to implement.

Here, we investigate the use of both kirigami and diamond-celled honeycomb structures to modify the stiffness of an ice-templated MFC plate and create a flexible self-sensing structure. Through the proposed manufacturing technique we can achieve high design freedom of the produced geometry, while describing a method that is scalable. We propose an extended honeycomb structure modeling technique based on Gibson *et al.* and derive a Young's modulus  $E^*$  for these MFC structures [17]. We select a particular geometry that is both flexible and light enough for our morphing wing application and functionalize it with a conductive ink. By measuring the change in resistance of this structure when different displacements are applied, we characterize its strain sensing behavior.

## II. MANUFACTURING

The manufacturing technique must allow for structural design freedom in order to reach the desired elasticity and the integration of self sensing capabilities. The following section describes this in more detail. All involved process steps are summarized in Fig. 3.

### A. Microfibrillated Cellulose

The MFC suspension was produced and characterized according to our previous work [27]–[29]. In brief, aqueous Eucalyptus pulp suspension was ground at a concentration of 2 wt% using an ultra-fine friction grinder “Supermass-colloider” (MKZA10-20 J CE, Masuko Sangyo Co., Ltd., Kawaguchi/Saitama, Japan) with a grinding energy input of 9 kWh/kg (referred to dry MFC content). After the grinding process, the MFC suspension was

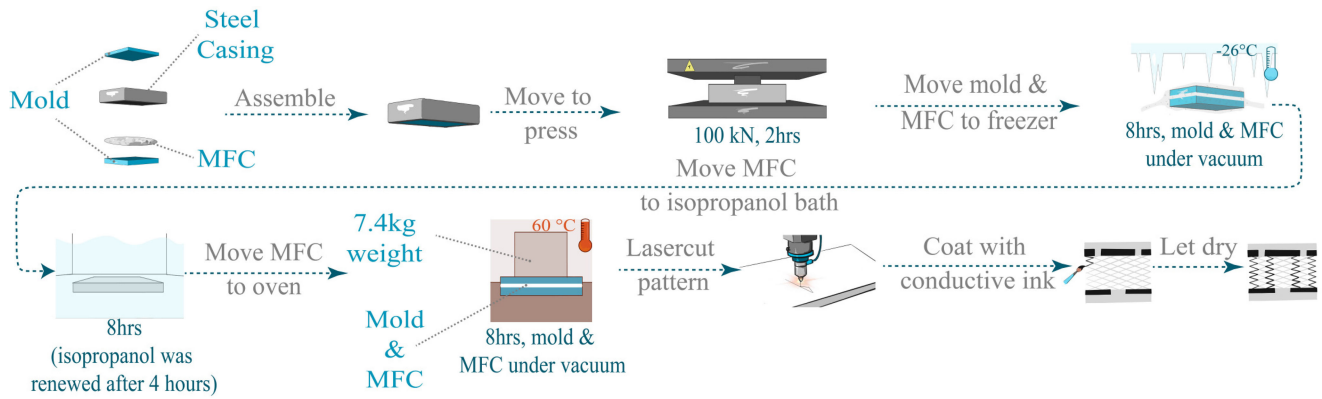


Fig. 3. Manufacturing process flowchart. After the mold is assembled, it is pressed and frozen while in a vacuum-bag. Afterwards, a solvent exchange is performed and the plate is dried. The plate is cut using a  $CO_2$  laser cutter and the conductive ink is applied.

dewatered with a sieve under pressure to reach a solid content of about 10–12 wt%. After bleaching the pulp to remove lignin and hemicellulose (done by the producer), the cellulose pulp was not chemically treated (i.e., non-oxidized) before mechanical disintegration.

### B. Ice-Templated Porous Microfibrillated Cellulose Structures

Molds were designed and manufactured to press the MFC into a rectangular shape and extract excessive water. They were printed using a commercial 3D printer from PLA. The mold consists of two flat components - a lower mold featuring integrated channels to allow water to flow during pressing and an upper mold to maintain a flat surface (inner geometry 100 mm  $\times$  100 mm). A steel casing holds the material between the two flat surfaces and determines the final thickness of the pressed plate (in our case 1.5 mm in the wet state). Placing a metal web on the lower mold allows the excessive water to be easily removed during pressing while maintaining a smooth surface. 78 g of MFC at a weight content of 12 wt% is spread uniformly by hand and the mold assembly is closed. Afterwards it is placed into a manual hydraulic press (4122 CE, Carver, Inc., Wabash, USA) and a linearly increasing pressure is applied over 15 minutes. Once a maximum force of 10 tons is reached, this force is maintained for 30 minutes. After 45 minutes of pressing, the pressure is relieved instantaneously, and the mold assembly is put into a vacuum bag. To maintain the geometry after pressing, vacuum is applied and the bag is sealed. The vacuum-bagged mold is placed into a freezer overnight at a temperature of  $-26^\circ\text{C}$ . Subsequently the frozen MFC part is extracted from the mold and put into an isopropanol solvent exchange bath for 8 hours. After 4 hours, the isopropanol is renewed to complete thawing and solvent exchange. The soaked MFC plate is placed in another 3D printed mold with the exact same dimensions. The assembly is put into a heated climate chamber for 8 more hours at a temperature of  $60^\circ\text{C}$ . During this time, a vacuum is drawn from the chamber to enable faster evaporation using a vacuum pump. To mitigate deflections that might appear during drying, a weight of 7.4 kg is placed on top of the mold. The finished dry plate of 1.2 mm thickness (ca. 50 % weight-content) is extracted from the mold and put into a climate chamber at 50 % RH and  $23^\circ\text{C}$  for at least 24 h.

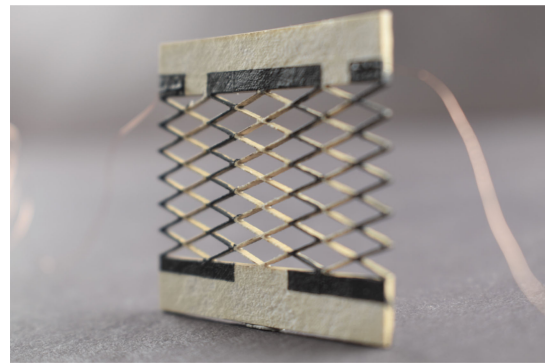


Fig. 4. Photograph of the realized honeycomb structure (40 mm  $\times$  36 mm) with an angle of  $\theta = 19.3^\circ$  and the attached cables.

### C. Manufacturing of Self Sensing Skin

The fully dried plate is placed in a  $CO_2$  laser cutter (Nova24 60 W, Thunder Laser Tech Co., Ltd., Shatian, China) to cut out the honeycomb geometry. During cutting, the speed of the laser is maximized to reduce the heat introduced to the structure while still achieving an acceptable resolution (60 % power,  $35 \frac{\text{mm}}{\text{sec}}$  cutting speed). After extracting the finished geometry it is masked using kapton tape so that one single “zig-zag” path is left free. A biodegradable conductive ink composed of carbon particles in a matrix of natural resin is manually coated on the structure. Two 80 cm long 0.01 mm diameter Copper wires are connected to the structure at both ends of the conductive path by using the ink as an adhesive. In order to dry the ink completely, the assembly is placed in an oven for 1 h at  $60^\circ\text{C}$ . An overview of the entire manufacturing process is given in Fig. 3 and the honeycomb geometry is shown in Fig. 4.

## III. CHARACTERIZATION

### A. Measurement Setup

Using two similar structures, we built a half-bridge Wheatstone setup that measures slight changes of resistance while applying strain to one of the structures. Using a 16-bit analogue-to-digital-converter in combination with a  $\mu$ -controller the bridge voltage can be measured with a sampling rate of up to 9600 Hz.

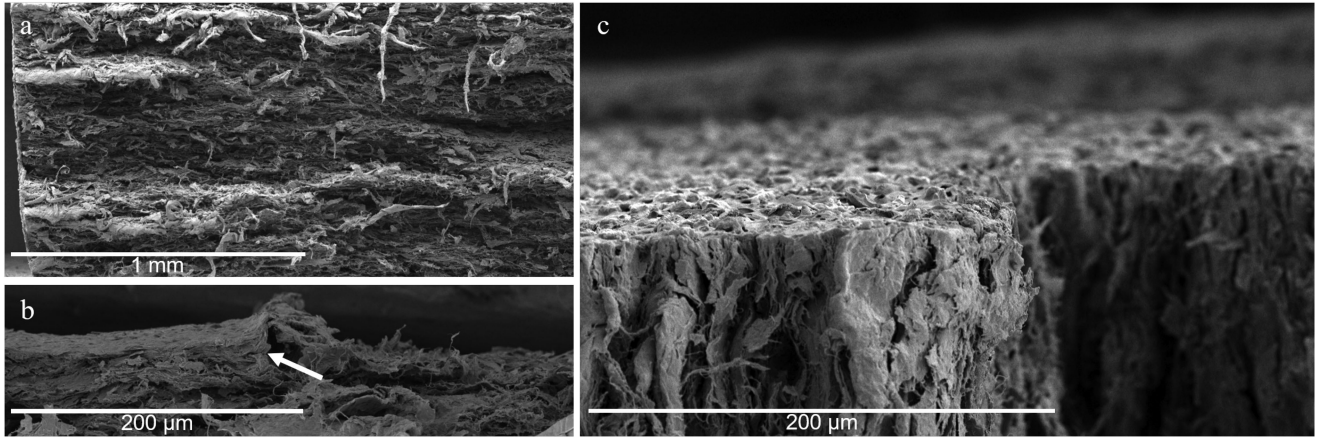


Fig. 5. SEM image of the material's fracture surface after freezing the plate using liquid nitrogen and manually breaking it. a) Cross-sectional view of the plate's morphology. b) Laser cut surface of the MFC plate. c) Interface of the conductive ink with the upper surface of the MFC plate. Arrow pointing at the added layer of ink. The right half is not coated and features a rougher surface than the left coated half.

### B. Microfibrillated Cellulose Mechanical Properties

To characterize the mechanical properties of the MFC plates, mechanical tests were performed. 4 ISO 527-2/5B samples were cut from each plate used to determine the Young's Modulus. The dogbone-shaped samples have been tested using a universal tensile testing machine (Z100 AllroundLine, ZwickRoell GmbH & Co. KG, Ulm, Germany) in combination with a 100 kN load-cell and manually screw grips. A mean Young's modulus of  $E_s = 2.28$  GPa ( $s = 0.11$  GPa) and a mean ultimate tensile strength of  $\sigma_M = 16.09$  MPa ( $s = 2.27$  MPa) were found. The rather large deviation of the tensile strength might be caused by structural inhomogeneities in the natural material used. This includes potentially inhomogeneous arrangement of fibrils, inhomogeneous fiber thickness and a locally varying proportion of non-fibrillated fibers.

The morphology of the MFC and the ink-MFC interface was monitored by scanning electron microscopy (Nova NanoSEM 230 instrument, FEI, Hillsboro, Oregon, USA) at an accelerating voltage of 5 keV. To gain insight into the cross-sectional area of the ink-coated MFC, the material was broken into two parts after freezing it using liquid nitrogen. The investigated samples were sputtered with 7 nm platinum (BAL-TEC MED 020 Modular High Vacuum Coating Systems, BAL-TEC AG, Liechtenstein). The resulting morphology is shown in Fig. 5a while the ink-MFC interface is given in Fig. 5b. The laser cut cellulose surface is shown in Fig. 5c. Due to the compression of the aqueous slurry in the press, the fibers are aligned orthogonal to the applied pressure and appear to be in layers (Fig. 5a). While ice-crystals form during the freezing step, cavities are created in the bulk material. During the solvent exchange, these cavities are filled with isopropanol and are thus prevented from collapsing. After drying and removing the solvent a porous and lightweight MFC plate is created. The average density of such structures is  $0.75 \frac{g}{cm^3}$  and the specific stiffness is  $3.04 \cdot 10^6 Pa / \frac{kg}{m^3}$ . Fig. 5c shows that laser cutting melts/burns the cellulose fibrils and creates a porous, flat surface. The ink that has been applied to the outer plane of the plate only infiltrates the upper section of the MFC and seals the fibrous surface. Compared to the un-coated surface, a smoother face is created.

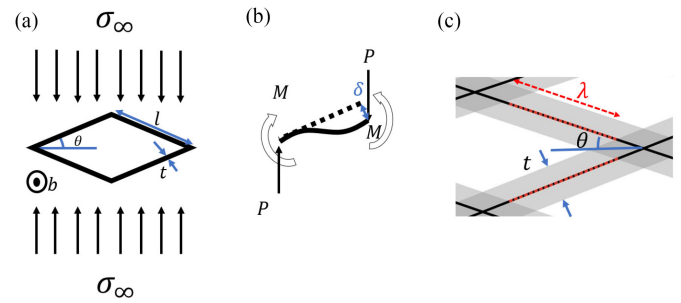


Fig. 6. Honeycomb loading condition and geometric constants for derivation of (2). a) a single cell loaded with far field stress  $\sigma_\infty$ . b) Free body diagram of a single cell wall. c) Honeycomb geometry corresponding to (3). The black lines represent the diamond with lines of length  $l$ , the gray represents the actual structure with thickness  $t$ , where the darker gray sections are where the cell walls overlap. The dashed red line is the midline of the beam of length  $\lambda$ .

### C. Honeycomb Homogenization

In order to reduce the stiffness of these MFC plates, the mechanics of diamond-celled honeycomb and kirigami structures were investigated. The purpose of this investigation is to determine how the stiffness of these structures varies based on their geometry. For diamond-celled honeycombs we are using the method described by Gibson et. al. [17] for modeling honeycomb structures. According to this method, each of the walls in the diamond cell can be approximated as a beam. This allows us to homogenize the structure by calculating the stress and strain on a single diamond cell. Ultimately, knowing this stress, and corresponding strain, allows us to treat our sensing structure as a sheet of material with a Young's modulus  $E_h^*$ .

When an entire diamond-celled honeycomb lattice is loaded uniaxially, each cell experiences a far field stress,  $\sigma_\infty$ . This stress state, depicted in Fig. 6a, causes the internal forces and moments shown in Fig. 6b. On a single cell wall,  $\sigma_\infty$  causes an internal force  $P$  and acts over the area  $lbcos(\theta)$ . This is the area that  $\sigma_\infty$  would act on if this honeycomb were a solid block of material. Given that the purpose of this analysis is to develop material constants so that it can be treated it as such,  $\sigma_\infty$  can be expressed by (1).

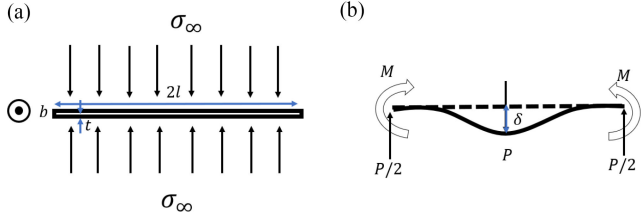


Fig. 7. Kirigami loading condition and geometric constants for derivation of (5). a) a single cell loaded with far field stress  $\sigma_\infty$ . b) Free body diagram of a single cell wall.

The amount that a single cell wall contributes to the overall length of a diamond-cell in the direction that  $\sigma_\infty$  is applied is  $l \sin(\theta)$ . Once that far-field stress,  $\sigma_\infty$ , is applied, the cell wall deflects by an amount  $\delta$ . This means that the length of the cell changes by  $\delta \cos(\theta)$ , resulting in an  $\epsilon$  given by (1). Using Euler-Bernoulli beam theory, one finds that  $\delta$  is given by (1), where  $E_s$  is the Young's modulus of the bulk material, and  $I$  is the area moment of the cell wall,  $bt^3/12$ .

$$\sigma_\infty = \frac{P}{lb \cos(\theta)}, \quad \epsilon = \frac{\delta \cos(\theta)}{l \sin(\theta)}, \quad \delta = \frac{P \cos(\theta) l^3}{12 E_s I} \quad (1)$$

If the honeycomb is treated as a linear-elastic material with constitutive relation  $\sigma = E_h^* \epsilon$ , one finds (2).

$$\frac{E_h^*}{E_s} = \left( \frac{t}{l} \right)^3 \frac{\sin(\theta)}{\cos^3(\theta)} \quad (2)$$

Similar forms of this expression have been documented for bi-modulus diamond-celled structures [30] and diagonally loaded square celled honeycombs [31]. However, this exact formulation could not be found, so to validate this, a series of finite element method (FEM) simulations were conducted in Abaqus/CAE 2019. Each of the cells were modeled with 20 shell elements along its length and 10 shell elements along its depth. A concentrated force was applied at each node along the lower edges of the honeycomb sample. The structure was constrained at the upper end from translating along the direction of the applied load and out of the honeycomb plate plane. Furthermore, those nodes were constrained from rotating about all axes. The structure was not constrained from translating within the plane of the honeycomb plate so as to neglect edge effects. Honeycomb theory assumes that the honeycomb has infinitely many cells in order to be properly homogenized. Allowing the cells to translate within this plane at the boundary provides the same affect as the honeycomb being infinitely long in the direction it is being loaded, but dramatically reduces computation time. A comparison of the FEM and analytical models is shown graphically in Fig. 8.

In these simulations, angles greater than  $45^\circ$  were not investigated. The model should still be valid at angles larger than  $45^\circ$ , but as the intention of this investigation is to reduce the stiffness and weight of the structure as much as possible, such larger angles are not relevant. In the case of  $\theta > 45^\circ$ , a structure of the same weight could be rotated by  $90^\circ$  and have a lower stiffness.

According to (2), as  $\theta$  approaches  $0^\circ$ , so does the Young's modulus of the honeycomb, which is a physical impossibility.

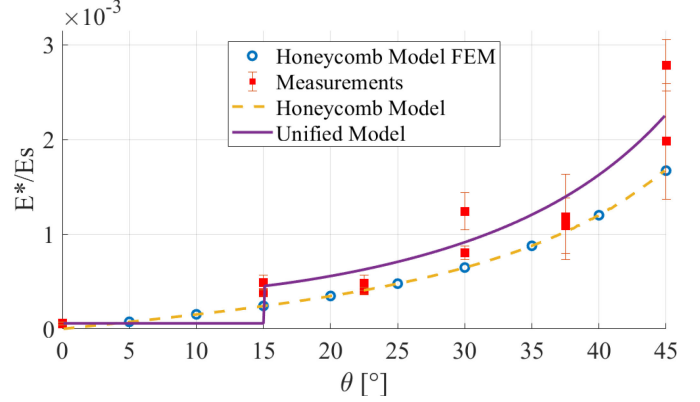


Fig. 8. Plot of the ratios determined using FEM on honeycomb structures with various angles of  $\theta$ , the actual measured ratios and their 95% confidence intervals, which are denoted as uncertainties, the initial honeycomb model shown in (2) and the unified model shown in (6).

This is because the affect of the thickness of each cell wall on the geometry is neglected. As such, (2) is modified to the following formulation

$$\frac{E_h^*}{E_s} = \left( \frac{t}{\lambda} \right)^3 \frac{\sin(\theta)}{\cos^3(\theta)} \quad \text{where,} \quad \lambda = l - \frac{t}{\sin(2\theta)} \quad (3)$$

In (3), the diamond cell with walls of length  $l$  is composed of beams of length  $\lambda$ . Here the regions where four of the cell walls overlap do not deform. This is depicted in Fig. 6c. This definition is in better agreement with our experimental results shown in Fig. 2.

The overlapping region is nearly negligible for large values of  $\theta$ , but as  $\theta$  decreases, this region becomes larger. Ultimately, our goal in using a diamond-celled honeycomb structure is to reduce both the weight and stiffness, however, at small values of  $\theta$  very little material is removed and the region of overlapping cell walls is so large that the stiffness does not decrease by very much. In cases where minimal stiffnesses are required, and the designer is less concerned about weight savings, a kirigami structure is preferable.

#### D. Kirigami Homogenization

The same modeling techniques used for diamond-celled honeycombs can also be used for kirigami structures. Investigations into how the stiffness of these structures changes with geometric parameters has been shown [15], but an explicit derivation of the Young's modulus of a sheet of material with a large number of kirigami slits,  $E_k^*$ , has not been demonstrated. In this case, each cell has a length  $2l$ , where each of the two cell walls in the kirigami structure are twice the length of the cell walls in an analogous honeycomb structure. If the same far field stress  $\sigma_\infty$  is applied to a sheet of material with the kirigami pattern, the resulting forces and moments acting on each beam are shown in Fig. 7. As a result, one finds (4).

$$\sigma_\infty = \frac{P}{2lb}, \quad \epsilon = \frac{\delta}{t/2}, \quad \delta = \frac{Pl^3}{24E_s I} \quad (4)$$

TABLE I  
 $E^*$  AND ELONGATION AT BREAK OF THE INVESTIGATED STRUCTURES

$\theta$ [°]	Specimen 1		Specimen 2	
	$E^*$ [MPa]	$\epsilon_b$ [%]	$E^*$ [MPa]	$\epsilon_b$ [%]
0	0.1193 ± 0.0051	96.38	0.1388 ± 0.0096	108.3
15	0.8666 ± 0.0141	44.09	1.116 ± 0.0186	61.87
22.5	0.9226 ± 0.0206	59.05	1.109 ± 0.0287	62.93
30	1.829 ± 0.0680	40.53	2.836 ± 0.0284	30.35
37.5	2.478 ± 0.0510	25.49	2.848 ± 0.0222	31.09
45	6.702 ± 0.0817	15.65	4.513 ± 0.2702	11.52

This leads to the final expression,

$$\frac{E_k^*}{E_s} = \frac{1}{2} \left( \frac{t}{l} \right)^4 \quad (5)$$

### E. Final Geometry and Unified Model

In testing various geometries, values of  $t = 0.50$  mm and  $l = 5.3$  mm were chosen in order to minimize the ratio of  $t/l$  within the constraints of our 100 mm × 100 mm plates and the tolerances of the laser cutter. Once this was decided, it was soon discovered that honeycomb structures with  $\theta < 15.0^\circ$  could not be accurately manufactured by the laser cutter. Furthermore, structures with these small angles have minimal stiffness reduction and are heavier than honeycombs at even slightly larger angles. As such, using a kirigami structure instead of a honeycomb with  $\theta < 15.0^\circ$  is far more reasonable. This results in the model shown in (6).

$$\frac{E^*}{E_s} = \begin{cases} \left( \frac{t}{\lambda} \right)^3 \frac{\sin(\theta)}{\cos^3(\theta)}, & \text{if } 15^\circ \leq \theta \leq 45^\circ \\ \frac{1}{2} \left( \frac{t}{l} \right)^4, & \text{otherwise} \end{cases} \quad (6)$$

## IV. RESULTS AND DISCUSSION

### A. Mechanical Analysis

To validate the accuracy of the developed unified model for the tensile stiffness of these structures, tensile tests were performed to determine the Young's modulus  $E^*$  and  $\epsilon_b$ . By doing so, honeycomb structures with different angles  $\theta$  were cut out from MFC plates and tested using a tensile testing machine (Z010 RetroLine, ZwickRoell GmbH & Co. KG, Ulm, Germany) and a 20 N load-cell. Fig. 8 shows the measured  $\frac{E^*}{E_s}$  ratios for the angles  $15.0^\circ$ ,  $22.5^\circ$ ,  $30.0^\circ$ ,  $37.5^\circ$ ,  $45.0^\circ$ , and the kirigami geometry (shown as  $0^\circ$ ) compared to the stiffness predicted by FEM, the honeycomb model and the unified model. Table I gives  $\epsilon_b$  and  $E^*$  of the different structures.

The specimens were clamped using pneumatic grips and pulled at a rate of  $1 \frac{mm}{min}$ , five times. The value of  $E^*$  was calculated by taking the slope of the stress and strain curve for each test. In order to calculate  $E_s$ , three tensile specimens were cut from different locations on the same plate. Those specimens were tested according to ISO 527-2/5B and the average  $E_s$  was calculated. These values were similar to the values discussed in section III-B. The error bars indicated in Fig. 8 give the 95% confidence intervals for each of the measurements. These confidence intervals account for the different values of  $E_s$  measured at different locations on the plate and the different values of  $E^*$  measured with the same specimen. To identify  $\epsilon_b$  the specimens

were tested according to ISO 527-1 at a rate of  $1 \frac{mm}{min}$ . In this test, we observed a general trend of increasing  $\epsilon_b$  with decreasing angle, with the exception of the specimens with  $\theta = 15^\circ$  and  $\theta = 22.5^\circ$ . We believe that this could either be the result of manufacturing inconsistencies by the laser cutter, or differences in stress concentration at the points where the cell walls meet caused by the varying geometry. A further investigation into this phenomenon is intended for future work.

From this experiment, we noted that the Young's modulus of the MFC plate was reduced by a factor ranging from 19 000 for the kirigami structure to 360 for the honeycomb structure with  $\theta = 45^\circ$ . The root mean square error (RMSE) between the unified model and the measured data is  $2.4 \times 10^{-4}$ . As the unified model is simply the honeycomb model at angles  $15.0^\circ < \theta < 45^\circ$  and the kirigami model for  $\theta < 15.0^\circ$ , it also makes sense to report the RMSE for each of these models. The RMSE for the honeycomb model (2) is  $2.6 \times 10^{-4}$  while the RMSE for the kirigami model (5) is  $4.8 \times 10^{-6}$ . The calculation of the RMSE values does not account for measurement uncertainty.

### B. Self-Sensing Characteristics

To investigate the self-sensing capabilities of the proposed structure, several mechanical tests were performed on a single specimen while measuring the Wheatstone bridge voltage. For those tests, the same setup as for the mechanical tests of the different angled honeycomb structures was used. A honeycomb structure with an angle of  $\theta = 19.3^\circ$  was investigated. This angle was chosen to comply with the competing requirement for a wing structure of having a suitable strength, while still being low in weight and enabling enough compliance to actuate the wing. To investigate the repeatability and response time of the sensing structure, a displacement of 1 mm at a rate of  $1 \frac{mm}{min}$  was applied to the structure. It was then returned to 0.05 mm displacement and held at this value for 30 seconds. 10 cycles of this loading and unloading were performed. Fig. 9a shows the measured bridge voltage during each of the 10 cycles, indicating that the sensor is slightly losing the capability to output the previously reached maximum bridge voltage. Taking into account that, over time, non-linear plastic effects in the MFC material and the ink might occur, the cycle's maximum voltage varies from the initial maximum of 19.67 mV by 0.71 % during the 2<sup>nd</sup> and 3<sup>rd</sup> cycle. A maximum deviation of 24.71 % was measured for the 9<sup>th</sup> cycle. This loss of maximum conductivity can be caused by cracks in the ink that do not close completely during unloading and therefore result in an unstable electrical path with higher resistivity. Fig. 9b provides an overview of the full measurement giving the applied displacement as well as the measured bridge voltage. It can be seen that the sensing structure outputs a linear signal which follows the applied displacement well at a response time that is lower than  $1 \frac{mm}{min}$ .

The sensitivity as well as the drift of the structure were investigated by applying and removing a step-wise displacement. In doing so, the sensor was displaced from 0 mm to 2 mm in 0.5 mm steps at a speed of  $1 \frac{mm}{min}$ . After reaching the expected displacements of 0 mm, 0.5 mm, 1 mm, 1.5 mm and 2 mm the values were held for 10 minutes. The bridge voltage together with the applied displacement during loading are given

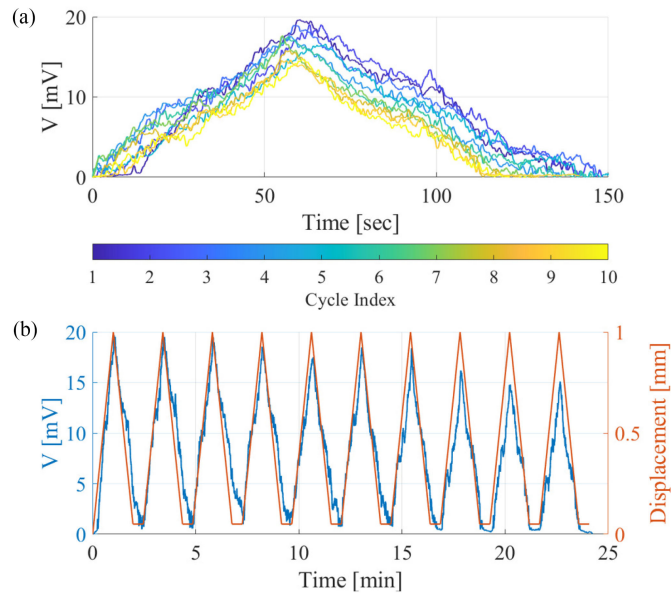


Fig. 9. The bridge voltage measured during cyclic loading and unloading of the coated  $\theta = 19.3^\circ$  honeycomb structure. a) Bridge voltage response during ten cycles. b) Bridge voltage response and applied displacement.

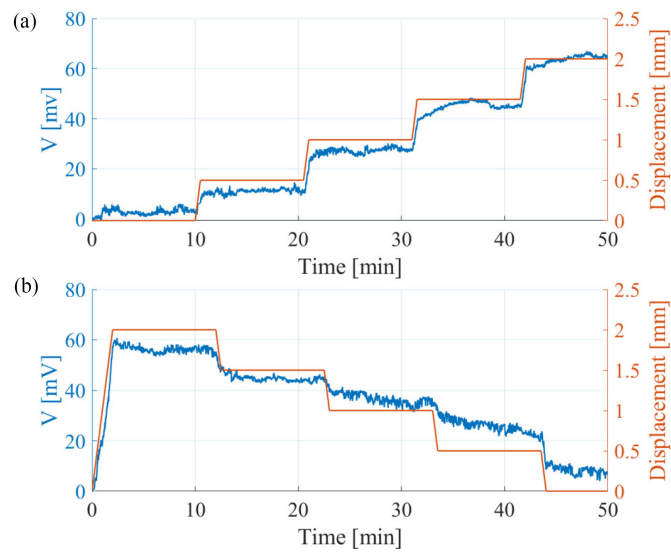


Fig. 10. The bridge voltage measured of the coated  $\theta = 19.3^\circ$  honeycomb structure while incrementally applying 0.5 mm of displacement and holding the individual strain for 10 minutes. a) Bridge voltage response during step wise increase of applied displacement. b) Bridge voltage response during step wise decrease of applied displacement.

in Fig. 10a while the bridge voltage and displacement during unloading are shown in Fig. 10b.

To visualize the sensor's performance a boxplot for each applied strain during loading (Fig. 11a) and unloading (Fig. 11b) is given. Applying a step-wise load to the structure resulted in a similar step-wise change in the measured bridge voltage. At smaller displacements (0 mm, 0.5 mm and 1 mm) the drift during the 10 minutes of holding is minimal, while it becomes moderate at 1.5 mm and 2 mm. It is assumed, that during high strains non-linear and time-dependent effects in the substrate and ink lead to a deviating bridge voltage. Over the period of the constant

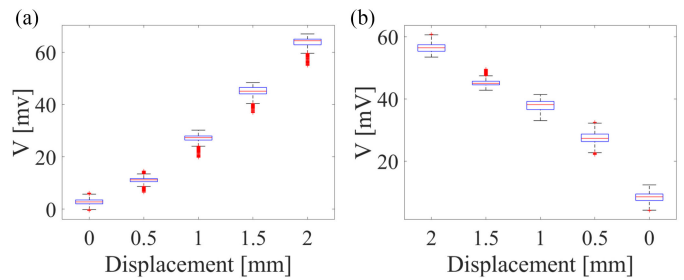


Fig. 11. The bridge voltage of the coated  $\theta = 19.3^\circ$  honeycomb structure visualized in a boxplot during the 10 minutes of holding the strain constant. a) Boxplot of bridge voltage during step-wise loading. b) Boxplot of bridge voltage during step-wise deloading.

strain, cracks in the ink can form at a varying rates, which leads to a non-constant bridge voltage. Therefore, during the step-wise unloading, the drift becomes more pronounced. This behavior might be caused by the high internal stresses at large displacements, which lead to a non-linear material response and local cracking of the ink. Such cracks would make the electrical path unstable. While reducing the displacement, the paths might not fully close again, and the resistance would neither follow a linear relationship nor stay at a constant level during constant strain. However, the strains in the manufactured sensor are within bounds, leading to good repeatability for short term applications. While the effects of temperature and humidity variation on the transducer have been canceled out using a half-bridge Wheatstone setup, changes in humidity might effect the structure's stiffness. While the ink was designed to be stable over a wide humidity range, the hydrophilic MFC substrate tends to swell in humid environments. It can be assumed that this affects the ink-substrate interaction and leads to an increased resistance. This effect is likely to be a dominant factor which needs to be accounted for in future work.

Applying a linear fit to the data presented in Fig. 11 the sensitivity was found to be  $31.45 \frac{mV}{mm}$  during loading ( $r^2 = 98.28\%$ ) and  $22.68 \frac{mV}{mm}$  during unloading ( $r^2 = 96.91\%$ ). Note that the true resolution is limited by the electronics used and corresponds to 0.125 mV or 0.05 mm. By conducting those tests we have been able to determine the resolution to be at least 0.5 mm of displacement, while measuring only moderate "noise". However, more detailed investigations are needed to study these phenomena.

### C. Future Work

We have observed that at high displacements the increased internal stress results in a non-uniform resistance response. We are assuming that cracking of the ink and the ink-MFC interface generates an unstable electrical path. Future work includes imaging of the conductive layer after applying cyclic loading and will focus on optimizing the ink's composition (e.g. adding plasticizer). Updating the printing technique (e.g. pad-printing) and using filtering tools on the measured signal would increase the sensing capabilities. Additional analyses need to be conducted to investigate the effect of the introduced heat flux by the laser cutter on the mechanical properties. Overall, the goal will be to advance this structure in terms of its mechanical and

sensing properties so that the aimed integration into a biodegradable morphing wing structure can be realized. To increase the service life beyond rather short one-way missions, the water barrier of the substrate needs to be enhanced, e.g. by applying a hydrophobic coating.

Moreover, we have presented a model for calculating the Young's modulus  $E^*$  when these structures are loaded in a single direction. Further investigation into these modeling techniques will involve derivation of the Young's moduli, shear moduli, and poisson's ratios in all directions such that a three-dimensional compliance matrix can be developed. This compliance matrix can be used in FEM models for aerial-robot components with complex geometries and multiple degrees of freedom. Furthermore, a more detailed investigation of the mechanics involved in  $\epsilon_b$  of these structures could provide further insights into how such values are affected by the structure's geometry and material properties.

## V. CONCLUSION

In this work we have presented a multi-step manufacturing method for producing lightweight and biodegradable structures made from MFC, that can be functionalized, while offering the ability to be upscaled. By applying a bio-inspired design approach and using honeycomb theory design techniques, we have been able to manufacture compliant bio-hybrid structures. We reduced the stiffness of the proposed structure by a factor of up to 19 000 and increased  $\epsilon_b$  by a factor of up to 113 compared to the bulk material made from cellulose fibrils - a material with a similar stiffness as Kevlar. By developing a mathematical model of diamond-honeycomb structures we provide a tool that is capable of predicting the mechanical behavior with less computationally effort for the proposed geometries. Coating the structure with a bio-based conductive ink, we integrated self-sensing capabilities that can give us feedback on the applied strain. Such bio-hybrid and self-sensing mechanisms with designed stiffness can be soft robotic building blocks for future sustainable eco-robots, which can operate and degrade in the environment and reduce e-waste. These results validate that cellulose based materials can be used for compliant soft robotic structures with self-sensing functionalization.

## ACKNOWLEDGMENT

We thank Anja Huch for preparing the SEM images and Marcel Rees and Walter Risi for providing the mechanical testing machine.

## REFERENCES

- [1] M. J. Harrington *et al.*, "Origami-like unfolding of hydro-actuated ice plant seed capsules," *Nat. Commun.*, vol. 2, no. 1, pp. 1–7, 6 2011.
- [2] E. E. Evke, D. Meli, and M. Shtein, "Developable rotationally symmetric kirigami-based structures as sensor platforms," *Adv. Mater. Technol.*, vol. 4, no. 12, 12 2019, Art. no. 1900563.
- [3] A. Baldwin and E. Meng, "A kirigami-based parylene c. stretch sensor," in *Proc. IEEE Int. Conf. Micro Electro Mech. Syst.*, 2017, pp. 227–230.
- [4] K. Xu, Y. Lu, S. Honda, T. Arie, S. Akita, and K. Takei, "Highly stable kirigami-structured stretchable strain sensors for perdurable wearable electronics," *J. Mater. Chem. C*, vol. 7, no. 31, pp. 9609–9617, 2019.
- [5] R. Sun *et al.*, "Kirigami stretchable strain sensors with enhanced piezoelectricity induced by topological electrodes," *Appl. Phys. Lett.*, vol. 112, no. 25, 2018, Art. no. 251904.
- [6] W. Zhou *et al.*, "Metal mesh as a transparent omnidirectional strain sensor," *Adv. Mater. Technol.*, vol. 4, no. 4, 2019.
- [7] C. Zheng, H. Oh, L. Devendorf, and E. Y.-L. Do, "Sensing kirigami," in *Proc. Designing Interactive Syst. Conf.*, 2019, pp. 921–934.
- [8] R. Ma, C. Wu, Z. L. Wang, and V. V. Tsukruk, "Pop-up conducting large-area biographene kirigami," *ACS Nano*, vol. 12, no. 10, pp. 9714–9720, 2018.
- [9] S. Chen, J. Chen, X. Zhang, Z.-Y. Li, and J. Li, "Kirigami/origami: Unfolding the new regime of advanced 3D microfabrication/nanofabrication with "folding"," *Light, Sci. Appl.*, vol. 9, no. 1, pp. 1–19, 2020.
- [10] A. Lamoureux, K. Lee, M. Shlian, S. R. Forrest, and M. Shtein, "Dynamic kirigami structures for integrated solar tracking," *Nature Commun.*, vol. 6, 2015, Art. no. 8092.
- [11] A. Rafsanjani, Y. Zhang, B. Liu, S. M. Rubinstein, and K. Bertoldi, "Kirigami skins make a simple soft actuator crawl," *Sci. Robot.*, vol. 3, no. 15, 2018.
- [12] S. Sareh and J. Rossiter, "Kirigami artificial muscles with complex biologically inspired morphologies," *Smart Mater. Structures*, vol. 22, no. 1, 2013, Art. no. 0 14004.
- [13] M. Cartolano, B. Xia, A. Miriyev, and H. Lipson, "Conductive fabric heaters for heat-activated soft actuators," *Actuators*, vol. 8, no. 1, 2019.
- [14] L. Guiducci *et al.*, "Honeycomb actuators inspired by the unfolding of ice plant seed capsules," *PLoS ONE*, vol. 11, no. 11, 2016.
- [15] D.-G. Hwang and M. D. Bartlett, "Tunable mechanical metamaterials through hybrid kirigami structures," *Sci. Rep.*, vol. 8, p. 3378, 2018.
- [16] M. Isobe and K. Okumura, "Initial rigid response and softening transition of highly stretchable kirigami sheet materials," *Sci. Reports*, vol. 6, 2016, Art. no. 24758.
- [17] L. J. Gibson, M. F. A. Sh, and J. G. S. Schajerj, "The mechanics of two-dimensional cellular materials," in *Proc. R. Soc. Lond. A*, vol. 382, 1982, pp. 25–42.
- [18] F. Cote, V. Deshpande, N. Fleck, and A. Evans, "The compressive and shear responses of corrugated and diamond lattice materials," *Internationa J. Solids Structures*, vol. 43, pp. 6220–6242, 2006.
- [19] Y. Forterre, J. M. Skotheim, J. Dumais, and L. Mahadevan, "How the venus flytrap snaps," *Nature*, vol. 433, pp. 421–425, 2005.
- [20] R. D. Allen, "Mechanism of the seismonastic reaction in mimosa pudica," *Plant Physiol.*, vol. 44, no. 8, pp. 1101–1107, 1969.
- [21] D. Michmizos and Z. Hiliotib, "A roadmap towards a functional paradigm for learning & memory in plants," *J. Plant Physiol.*, vol. 232, pp. 209–215, 2019.
- [22] A. Trewavas, "Green plants as intelligent organisms," *TRENDS Plant Sci.*, vol. 10, no. 9, pp. 413–419, 2005.
- [23] A. Baldwin and E. Meng, "Kirigami strain sensors microfabricated from thin-film parylene c," *J. Microelectromech. Syst.*, vol. 27, no. 6, pp. 1082–1088, 2018.
- [24] J. Luo, Y. Yao, X. Duan, and T. Liu, "Force and humidity dual sensors fabricated by laser writing on polyimide/paper bilayer structure for pulse and respiration monitoring," *J. Mater. Chem. C*, vol. 6, no. 17, pp. 4727–4736, 2018.
- [25] S. Laflamme, M. Kollosche, J. J. Connor, and G. Kofod, "Robust flexible capacitive surface sensor for structural health monitoring applications," *J. Eng. Mechanics*, vol. 139, no. 7, pp. 879–885, 2013.
- [26] A. Guemes, A. Fernandez-Lopez, A. R. Pozo, and J. Sierra-Perez, "Structural health monitoring for advanced composite structures: A review," *J. Composites Sci.*, vol. 4, no. 1, pp. 1–15, 2020.
- [27] S. Josset and G. Siqueira, "Energy consumption of the nanofibrillation of bleached pulp, wheat straw and recycled newspaper through a grinding process porous nanofibrillated cellulose functional materials view project wendeliterature view project," *Article Nordic Pulp Paper Res. J.*, 2014.
- [28] S. Josset *et al.*, "Microfibrillated cellulose foams obtained by a straight-forward freeze-thawing-drying procedure," *Cellulose*, vol. 24, no. 9, pp. 3825–3842, 2017.
- [29] C. Antonini *et al.*, "Ultra-porous nanocellulose foams: A facile and scalable fabrication approach," *Nanomaterials*, vol. 9, no. 8, 2019.
- [30] H. Hatami-Marbini and M. Rohanifar, "Stiffness of bi-modulus hexagonal and diamond honeycombs," *J. Mech. Sci. Technol.*, vol. 33, no. 4, pp. 1703–1709, 2019.
- [31] A.-J. Wang and D. L. McDowell, "In-plane stiffness and yield strength of periodic metal honeycombs," *J. Eng. Mater. Technol.*, vol. 126, pp. 137–156, 2004.